



# Sympathetic Solar Eruption on 2024 February 9

Shu-Yue Li<sup>1,2</sup>, Qing-Min Zhang<sup>2</sup>, Bei-Li Ying<sup>2</sup>, Li Feng<sup>2</sup>, Ying-Na Su<sup>2</sup>, Mu-Sheng Lin<sup>2,3</sup>, and Yan-Jie Zhang<sup>2</sup>

<sup>1</sup>School of Science, Nanjing University of Posts and Telecommunications, Nanjing 210023, China

<sup>2</sup>Key Laboratory of Dark Matter and Space Astronomy, Purple Mountain Observatory, Nanjing 210023, China; [zhangqm@pmo.ac.cn](mailto:zhangqm@pmo.ac.cn)

<sup>3</sup>School of Astronomy and Space Science, University of Science and Technology of China, Hefei 230026, China

Received 2024 November 04; revised 2024 November 28; accepted 2024 November 29; published 2025 January 2

## Abstract

In this paper, we perform a follow-up investigation of the solar eruption originating from active region 13575 on 2024 February 9. The primary eruption of a hot channel generates an X3.4 class flare, a full-halo coronal mass ejection (CME), and an extreme-ultraviolet (EUV) wave. Interaction between the wave and a quiescent prominence (QP) leads to a large-amplitude, transverse oscillation of QP. After the transverse oscillation, QP loses equilibrium and rises up. The ascending motion of the prominence is coherently detected and tracked up to  $\sim 1.68 R_{\odot}$  by the Solar UltraViolet Imager onboard the GOES-16 spacecraft and up to  $\sim 2.2 R_{\odot}$  by the Solar Corona Imager (SCI\_UV) of the Ly $\alpha$  Solar Telescope onboard the ASO-S spacecraft. The velocity increases linearly from 12.3 to 68.5 km s<sup>-1</sup> at 18:30 UT. The sympathetic eruption of QP drives the second CME with a typical three-part structure. The bright core comes from the eruptive prominence, which could be further observed up to  $\sim 3.3 R_{\odot}$  by the Large Angle Spectroscopic Coronagraph onboard the Solar and Heliospheric Observatory mission. The leading edge of the second CME accelerates continuously from  $\sim 120$  to  $\sim 277$  km s<sup>-1</sup>. The EUV wave plays an important role in linking the primary eruption with the sympathetic eruption.

*Key words:* Sun: flares – Sun: filaments, prominences – Sun: coronal mass ejections (CMEs)

## 1. Introduction

Filaments are widespread in the solar corona (Engvold 1998; Mackay et al. 2010; Parenti 2014). They consist of very dynamic and dark threads observed in the H $\alpha$  line center (Martin 1998; Lin 2011). Above the limb, filaments are called prominences, which show bright features due to their strong emissions in H $\alpha$  (6562.8 Å), Ca II H line (3968 Å), H I Ly $\alpha$  (1216 Å), and He II (304 Å) wave bands (Berger et al. 2008; Zhou et al. 2023; Qiu et al. 2024; Xue et al. 2024). After being disturbed, the filament threads tend to deviate from their equilibrium positions and oscillate for a few cycles before calming down (Oliver & Ballester 2002; Tripathi et al. 2009; Arregui et al. 2018).

According to the velocity amplitude, filament oscillations are divided into small-amplitude ( $\leq 10$  km s<sup>-1</sup>) oscillations (SAOs) and large-amplitude ( $\geq 20$  km s<sup>-1</sup>) oscillations (LAOs). SAOs are frequently observed in quiescent prominences (QPs; Okamoto et al. 2007; Ning et al. 2009; Li et al. 2018; Wang et al. 2024). LAOs are occasionally detected in active region (AR) filaments as well as quiescent filaments (Shen et al. 2014a; Luna et al. 2018, 2024). Based on the direction of oscillations, LAOs are further divided into longitudinal and transverse oscillations. The filament materials move along the threads during longitudinal oscillations (Jing et al. 2003; Vršnak et al. 2007; Zhang et al. 2012, 2017; Zheng et al. 2017; Ni et al. 2022). On the contrary, the filament threads swing back and forth perpendicularly to the spine during transverse

oscillations (Isobe & Tripathi 2006; Hershaw et al. 2011; Dai et al. 2023; Zhang et al. 2024). Shen et al. (2014b) discovered simultaneous transverse oscillations of one filament and longitudinal oscillations of another one induced by a single shock wave. Longitudinal and transverse oscillations before eruptions have been observed (Isobe & Tripathi 2006; Bi et al. 2014; Zhang et al. 2020; Dai et al. 2021; Ni et al. 2022), which make LAOs a credible precursor for filament eruptions considering that LAOs may stand for a transition phase between the initial equilibrium and the eventual eruption (Chen et al. 2008; Zhang et al. 2012; Fan 2020).

Filament eruptions are intimately related with solar flares (Fletcher et al. 2011) and coronal mass ejections (CMEs; Forbes et al. 2006; Chen 2011) in the standard flare model, namely the CSHKP model (Carmichael 1964; Sturrock 1966; Hirayama 1974; Kopp & Pneuman 1976). Owing to the magnetic connectivity between two or three filaments, the eruption of a primary filament may considerably affect the environment of another filament and lead to a second eruption, which is considered as a sympathetic eruption. The most commonplace condition for a sympathetic eruption is that multiple filaments are suppressed by a common, overlying magnetic system. Successful eruption of the first filament may significantly reduce the constraint on the adjacent filaments and trigger a second or even a chain of eruptions (Sterling & Moore 2004; Cheng et al. 2005, 2013; Shen et al. 2012; Yang et al. 2012; Lynch & Edmondson 2013; Joshi et al. 2016;

Wang et al. 2016, 2018; Dacie et al. 2018; Hou et al. 2020; Song et al. 2020; Zhou et al. 2021). Török et al. (2011) performed a three-dimensional (3D) magnetohydrodynamics (MHD) simulation to explore possible magnetic trigger mechanisms for sympathetic eruptions. In their model, two magnetic flux ropes (MFRs) are located within a pseudo-streamer and the third one is located nearby. The eruption of the third rope gives rise to consecutive eruptions of the two MFRs, which could excellently explain the observed twin filament eruptions and CMEs on 2010 August 1 (Titov et al. 2012). Shen et al. (2012) studied two sympathetic filament eruptions including a partial and full MFR eruptions in a quadrupolar magnetic configuration on 2011 May 12. A schematic model is proposed to illustrate the whole process. Breakout magnetic reconnection occurs after the first filament rises up, which finally evolves into a CME. The adjacent filament undergoes a partial eruption, with the top part evolving into a blob.

Impulsive eruptions are likely to drive coronal extreme-ultraviolet (EUV) waves (Thompson et al. 1998; Chen et al. 2002; Patsourakos & Vourlidas 2009) or chromospheric Moreton waves (Moreton 1960; Eto et al. 2002), which propagate away at speeds of hundreds of  $\text{km s}^{-1}$  to  $\sim 1000 \text{ km s}^{-1}$ . Interactions between these global waves and remote filaments may result in LAOs (Gilbert et al. 2008; Hershaw et al. 2011; Asai et al. 2012; Liu et al. 2013; Dai et al. 2023; Zhang et al. 2024) or direct eruptions. Jiang et al. (2011) investigated three successive filament eruptions from different locations on 2003 November 19. The first eruption originates from AR 10501 and generates a CME. The CME-related coronal dimmings propagate outward and interact with two quiescent filaments, leading to the second and third eruptions and related flares. It is concluded that the dimming process in the first eruption results in weakening and partial removal of the large-scale, overlying magnetic fields on the two remote filaments, which facilitate sympathetic eruptions. Dai et al. (2021) studied the sympathetic eruption of a very long quiescent filament excited by the eruption of a nearby smaller filament on 2015 April 28. The two parallel filaments are  $\sim 250 \text{ Mm}$  apart. Prior to the sympathetic eruption, the huge filament undergoes both longitudinal and transverse oscillations, which are accompanied by continuous mass drainage at speeds of  $35\text{--}85 \text{ km s}^{-1}$ . The combination of LAOs and mass drainage indicates that the filament is losing equilibrium gradually. Till now, a complete process of LAOs and the subsequent sympathetic eruption of a prominence excited by EUV waves has not been reported. Using multiwavelength observations of the Atmospheric Imaging Assembly (AIA; Lemen et al. 2012) onboard the Solar Dynamics Observatory (SDO; Pesnell et al. 2012), Zhang et al. (2024) (hereafter Paper I) studied two successive EUV waves and the induced transverse oscillation of a QP on 2024 February 9. The EUV waves are separately driven by a fast halo CME<sup>4</sup> (hereafter

**Table 1**  
Wavelengths, Pixel Sizes, Cadences, and FOVs of the Instruments on 2024 February 9

Instrument	$\lambda$ ( $\text{\AA}$ )	Pixel Size (arcsec)	Cadence (s)	FOV ( $R_{\odot}$ )
SDO/AIA	211	0.6	12	$\sim 1.3$
GOES-16/SUVI	304	2.5	$\sim 120$	$\sim 1.6$
GOES-16/SUVI	171	2.5	240	$\sim 1.6$
GOES-16	1–8	...	1	...
ASO-S/SCI_UV	1216	2.15	$\sim 60$	1.1–2.5
SOHO/LASCO-C2	WL	11.4	720	2–6
SOHO/LASCO-C3	WL	56.0	720	4–30
STA/COR2	WL	15	900	2.5–15

CME1) as a result of a hot channel (HC) eruption and by a fast coronal jet originating from AR 13575. QP is close to the solar south pole and is more than  $380 \text{ Mm}$  away from the flare site.

In this paper, using EUV observations of the Solar UltraViolet Imager (SUVI; Seaton & Darnel 2018; Tadikonda et al. 2019; Darnel et al. 2022) onboard the Geostationary Operational Environmental Satellite (GOES-16) and ultraviolet (UV;  $121.6 \pm 10 \text{ nm}$ ) observations of the Solar Corona Imager (SCI\_UV) of the Ly $\alpha$  Solar Telescope (LST; Feng et al. 2019; Li et al. 2019; Chen et al. 2024) onboard the Advanced Space-based Solar Observatory (ASO-S; Gan et al. 2019, 2023), we reanalyze the event, focusing on the sympathetic eruption of QP and the related CME (hereafter CME2). Characteristics of these instruments are summarized in Table 1. In Section 2, we briefly describe the data analysis of these instruments. In Section 3, we first show the primary eruption, which leads to an X3.4 flare, CME1, and an EUV wave. Then, we show the sympathetic eruption of QP, which leads to CME2 without a flare. Discussions and a brief summary are arranged in Sections 4 and 5, respectively.

## 2. Data Analysis

SDO/AIA takes full-disk images in seven EUV (94, 131, 171, 193, 211, 304, and  $335 \text{ \AA}$ ) and two UV (1600 and  $1700 \text{ \AA}$ ) wavelengths. The level\_1 data are calibrated using the standard program `aia_prep.pro` in the *Solar Software* package. The full-disk GOES-16/SUVI images in 171 and  $304 \text{ \AA}$  are rotated and slightly shifted to align with the AIA images (Zhang et al. 2024). The Ly $\alpha$  images from ASO-S/SCI\_UV are primarily processed through the correction of flat fields and dark currents, along with the normalization of exposure times. To suppress stray light signals, we subtract the daily-minimum background from the images. Following this, the images are rotated, scaled, and aligned by overlapping structures in the field of view (FOV) with the AIA  $304 \text{ \AA}$  images. The high cadence and large FOV of ASO-S/SCI\_UV provide a great opportunity to track the erupting prominence from  $\sim 1.1$  to  $\sim 2.2 R_{\odot}$  in Ly $\alpha$  wavelength. The white-light (WL) images of CMEs are

<sup>4</sup> [https://cdaw.gsfc.nasa.gov/CME\\_list/UNIVERSAL\\_ver2/2024\\_02/univ2024\\_02.html](https://cdaw.gsfc.nasa.gov/CME_list/UNIVERSAL_ver2/2024_02/univ2024_02.html)

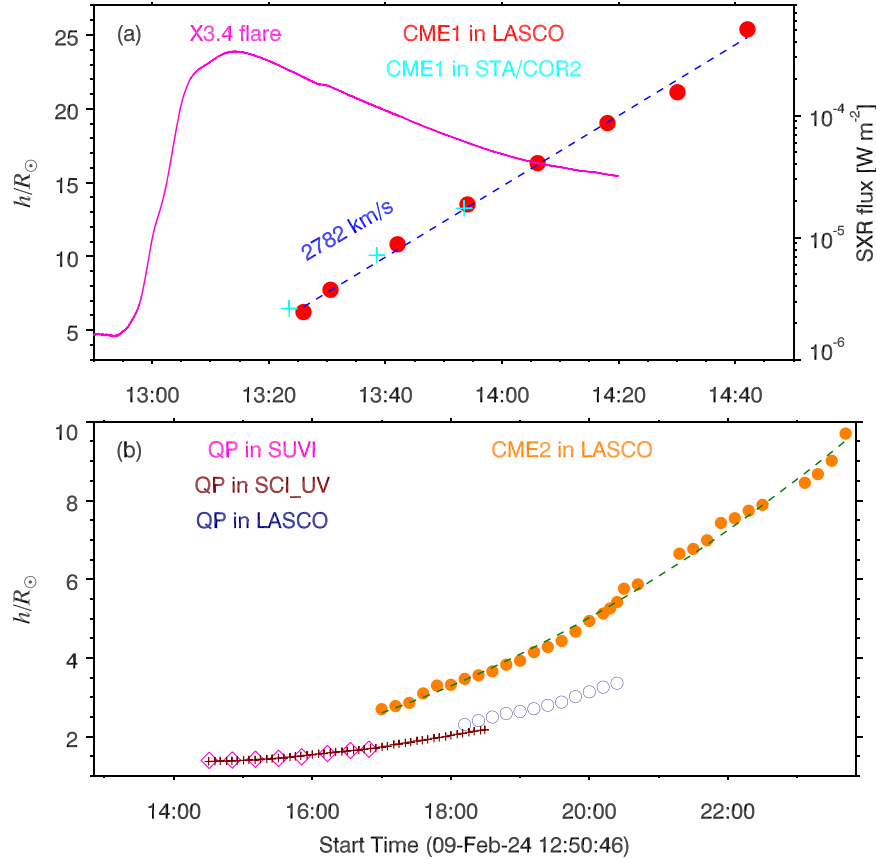


**Figure 1.** (a) SXR light curve of the X3.4 class flare in  $1-8 \text{ \AA}$  (magenta line) and height evolutions of CME1 in LASCO (red circles) and STA/COR2 (cyan pluses). A linear fitting is performed with a velocity of  $\sim 2782 \text{ km s}^{-1}$  for CME1 in the FOV of LASCO. (b) Height evolutions of QP in SUVI (magenta diamonds), SCI\_UV (brown pluses), and LASCO (blue circles). Height evolution of CME2 is plotted with orange circles and fitted with a quadratic function (green dashed line).

obtained from the C2 and C3 coronagraphs of the Large Angle Spectroscopic Coronagraph (LASCO; Brueckner et al. 1995) onboard the Solar and Heliospheric Observatory (SOHO) mission as well as the COR2 coronagraph onboard the ahead Solar TERrestrial RELations Observatory (Kaiser et al. 2008).

### 3. Results

#### 3.1. Primary Eruption

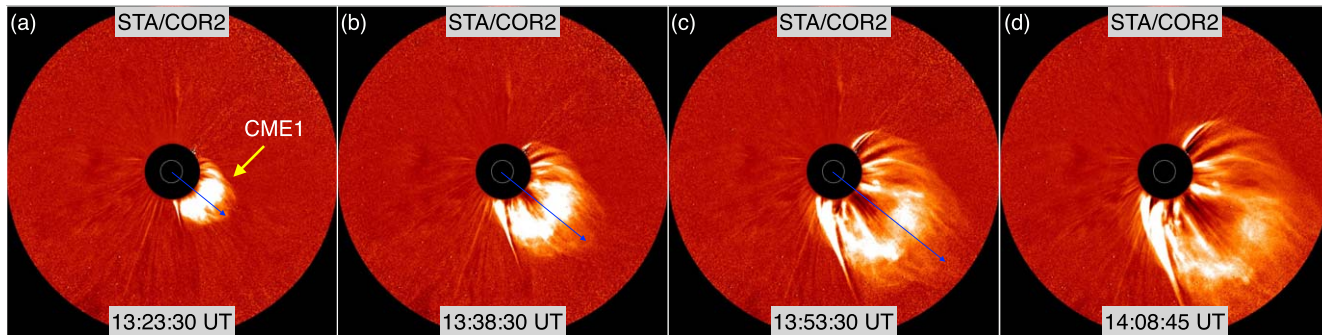
As shown in Figures 3 and 5 of Paper I, the HC is exclusively observed in 131 and  $94 \text{ \AA}$  of SDO/AIA. It undergoes a slow rise phase and a fast rise phase, the latter of which starts from 12:53:53 UT and lasts for  $\sim 10$  minutes before escaping the FOV of AIA. In Figure 1(a), the soft X-ray (SXR) light curve of the flare in  $1-8 \text{ \AA}$  recorded by the GOES-16 spacecraft is plotted with a magenta line. The SXR emission increases from 12:53 UT and peaks at 13:14 UT before declining gradually.

Figure 2 shows four running-difference images observed by STA/COR2, which had a separation angle of  $7.6^\circ$  with the

Sun–Earth connection on 2024 February 9. In panel (a), the yellow arrow points to CME1 when it first appears at 13:23:30 UT. CME1 propagates in the southwest direction and expands rapidly to form a full-halo CME (panels (b)–(d)). In panels (a)–(c), the blue arrows indicate the propagation direction and heliocentric distances of the CME leading edge, which are plotted with cyan pluses in Figure 1(a).

As is shown in the bottom panels of Figure 3 in Paper I, CME1 was also observed by SOHO/LASCO. The height variation of CME1 with time in the FOV of SOHO/LASCO is plotted with red circles in Figure 1(a). A linear fitting is performed between 13:25 UT and 14:45 UT, which is displayed with a blue dashed line. The apparent speed of CME1 reaches  $\sim 2782 \text{ km s}^{-1}$  in the plane of the sky.

In Figure 3, panels (a)–(c) show base-difference images in AIA  $211 \text{ \AA}$  during 13:05–13:09 UT (see also Figure 6 in Paper I). QP is signified by black rectangles. Panel (d) shows the GOES-16/SUVI  $304 \text{ \AA}$  image at 13:09:06 UT, featuring the columnar QP near the south polar region. The quick expansion of CME1 generates an EUV wave front (WF1),



**Figure 2.** CME1 observed by STA/COR2 during 13:23–14:09 UT. The blue arrows indicate the propagation direction and heliocentric distances of the CME leading edge.

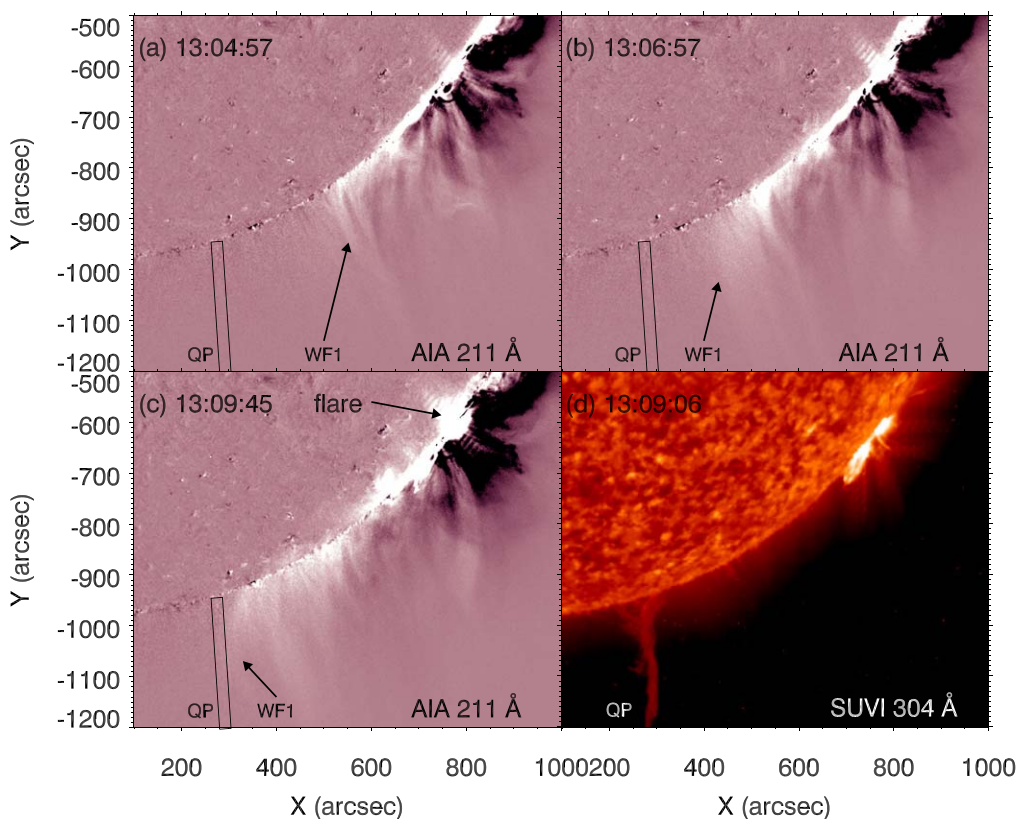


**Figure 3.** (a)–(c) AIA 211 Å base-difference images, showing the flare and EUV wave front (WF1). The position of QP is signified by black rectangles. (d) SUVI 304 Å image at 13:09:06 UT, showing the columnar QP near the south polar region.

which is indicated by black arrows. WF1 propagates in the southeast direction at a speed of  $\sim 835 \text{ km s}^{-1}$  and arrives at the prominence at  $\sim 13:09$  UT (panel (c)).

The left panels of Figure 4 show the QP with a position angle (PA) of  $\sim 196^\circ$ , which is observed by SUVI 304 and 171 Å around 12:49 UT. The width and height of QP in 304 Å are  $\sim 17.4 \text{ Mm}$  and  $\sim 188 \text{ Mm}$ , respectively. Therefore, the aspect ratio of QP is  $\sim 11$ .

The strong impact of WF1 excites a transverse oscillation of QP. In the left panels of Figure 4, a straight slice (S1) perpendicular to the prominence is selected to study the oscillation. Time–distance diagrams of S1 in 304 and 171 Å are displayed in the left panels of Figure 5. The magenta and cyan dashed lines indicate peak times ( $\sim 13:21$  UT and  $\sim 13:43$  UT) of the transverse oscillation. It is clear that QP swings back and forth for two cycles with an initial amplitude and a period of

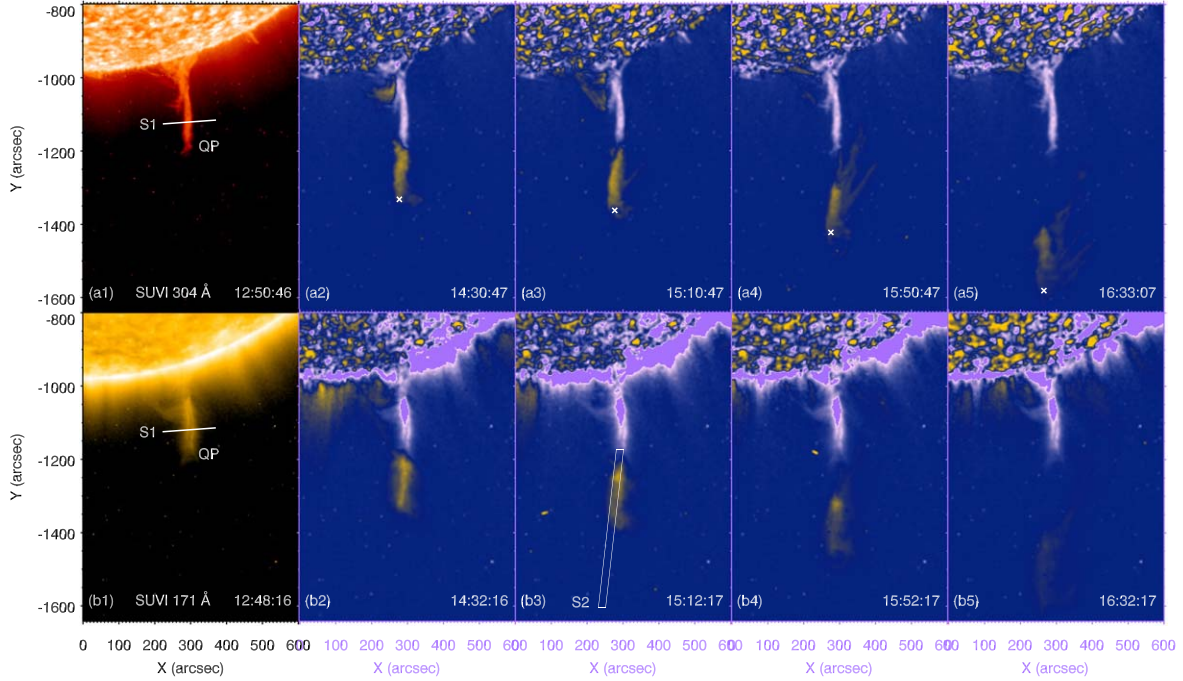


**Figure 4.** Top panels: SUVI 304 Å original image at 12:50:46 UT and base-difference images during 14:30–16:33 UT. The white crosses mark the leading edges of QP. Bottom panels: SUVI 171 Å original image at 12:48:16 UT and base-difference images during 14:32–16:32 UT. The slice (S1) in the left panels is used to study the transverse oscillation of QP. The wide slice (S2) in panel (b3) is used to study the rising motion of QP. An online animation of the 304 and 171 Å base-difference images is available at [anim1.mp4](#). The  $\sim 6$  s animation covers from 12:50 UT to 16:50 UT.

$\sim 27$  Mm and  $\sim 25$  minutes respectively. It is worth mentioning that variations of the initial amplitudes, velocities, and periods with the prominence height are demonstrated in Figure 10 of Paper I.

### 3.2. Sympathetic Eruption of QP

The transverse oscillation lasts for up to  $\sim 60$  minutes until 14:09 UT. Then, QP breaks into two pieces. The top part lifts off to form CME2, while the lower part remains and collapses gradually. Base-difference images in SUVI 304 and 171 Å during 14:30–16:33 UT are displayed in panels (a2)–(a5) and panels (b2)–(b5) of Figure 4 respectively (see also the online movie anim1.mp4 available as Supplementary material). It is obvious that as QP rises up, a fraction of plasmas falls back to the solar surface. The leading edges of QP in 304 Å are marked with white crosses. In Figure 1(b), the magenta diamonds correspond to the heliocentric distances of the prominence leading edges, which increase from  $\sim 1.40R_{\odot}$  to  $\sim 1.68R_{\odot}$  during 14:30–16:50 UT.

In Figure 4(b3), a wide slice (S2) is selected along the propagation direction of QP. It is evident that QP propagates non-radially with an inclination angle of  $\sim 23^{\circ}$  with respect to the local vertical direction (Zhang et al. 2022). Time-slice diagrams of S2 in 304 and 171 Å are displayed in the right panels of Figure 5. It is seen that QP is accelerating during the

eruption. As is shown in Table 1, SUVI has an FOV of  $\sim 1.6R_{\odot}$ . The erupting QP becomes blurred and fades out after 16:50 UT in SUVI images. Fortunately, it is captured by the ASO-S/SCI\_UV coronagraph with a much larger FOV of  $\sim 2.5R_{\odot}$  and a much higher time cadence. Figure 6 shows QP observed by SCI\_UV during 14:30–18:20 UT (see also the online movie anim2.mp4 available as Supplementary material). The shape of the prominence changes from a column to a hook as it ascends. Likewise, temporal evolution of the heliocentric distances of QP in the FOV of SCI\_UV are drawn with brown pluses in Figure 1(b) and excellently fitted with a quadratic function

$$\frac{h_{\text{QP}}(t - t_0)}{R_{\odot}} = 1.36 + 1.77 \times 10^{-5}(t - t_0) + 2.80 \times 10^{-9}(t - t_0)^2, \quad (1)$$

where  $t_0$  is set to be 14:30:12 UT.  $h_{\text{QP}}$  increases slowly from  $\sim 1.37R_{\odot}$  and accelerates to  $\sim 2.18R_{\odot}$  at 18:29:27 UT. The apparent speed of QP is  $v_{\text{QP}}(t - t_0) = 12.3 + 3.9 \times 10^{-3}(t - t_0) \text{ km s}^{-1}$ . Hence,  $v_{\text{QP}}$  increases slowly from  $12.3 \text{ km s}^{-1}$  at 14:30 UT to  $68.5 \text{ km s}^{-1}$  at 18:30 UT.

Figure 7 shows five original images observed by LASCO-C2 during 17:00–20:12 UT. CME2 presents a typical three-part structure (Illing & Hundhausen 1985; Song et al. 2022). The bright front of CME2, which is pointed out by the yellow

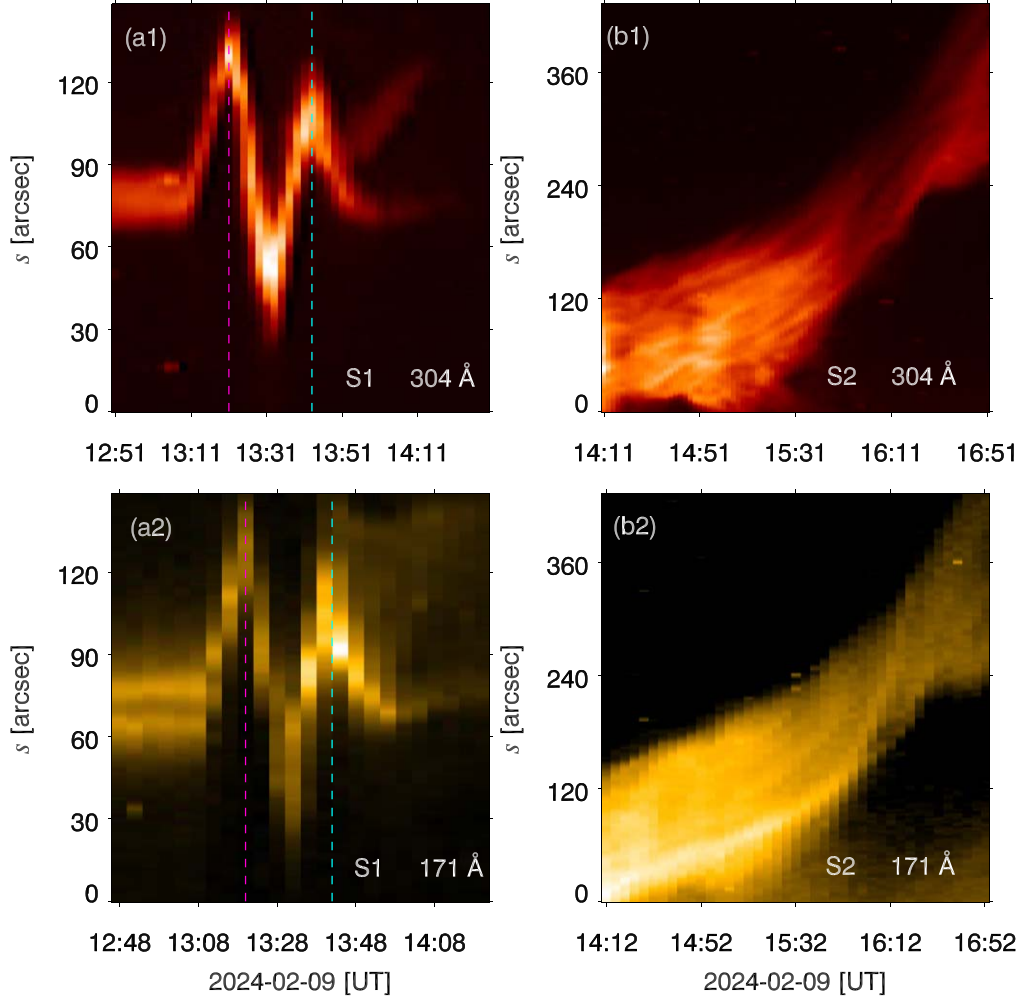


**Figure 5.** Time–distance diagrams of S1 (left panels) and S2 (right panels) in SUVI 304 Å (top panels) and 171 Å (bottom panels). The magenta and cyan dashed line indicate peak times of the transverse oscillation.

arrow, turns up at 17:00 UT and propagates in the south direction with a PA of  $190^\circ$  (panels (a)–(b)). At 18:12 UT, the bright core of CME2 appears. Considering that CME2 is driven by the erupting QP, QP is exactly the core of CME2, which is pointed out by an orange arrow (panel (c)). Afterwards, QP and the bright front of CME2 move outward together (panels (d)–(e)). In Figure 1(b), temporal evolution of the heliocentric distances of QP in the FOV of LASCO-C2 is plotted with blue circles. It is obvious that QP evolves coherently in the FOVs of SCI\_UV and LASCO-C2. The slight difference in height during 18:12–18:30 UT is probably due to the different wavelengths. QP is observed in UV ( $121.6 \pm 10$  nm) by SCI\_UV and in WL by LASCO-C2. The advantages of passband and large FOV of SCI\_UV enable us to track erupting prominences completely from their early phases up to  $\sim 2.5 R_\odot$ . In Figure 1(b), temporal evolution of the heliocentric

distances of the bright front is plotted with orange circles. Similarly, the trajectory is satisfactorily fitted with a quadratic function

$$\frac{h_{\text{CME2}}(t - t_2)}{R_\odot} = 2.60 + 1.73 \times 10^{-4}(t - t_2) + 4.70 \times 10^{-9}(t - t_2)^2, \quad (2)$$

where  $t_2$  is set to be 17:00:00 UT. Likewise, the apparent speed of CME2 is  $v_{\text{CME2}}(t - t_2) = 120.4 + 6.5 \times 10^{-3}(t - t_2)$  km s $^{-1}$ . Therefore,  $v_{\text{CME2}}$  increases gradually from 120.4 km s $^{-1}$  at 17:00 UT to 277.2 km s $^{-1}$  at 23:42 UT.

The whole sequence of events, including the X3.4 flare, CME1, coronal jet, EUV wave fronts (WF1 and WF2), QP, and CME2, is illustrated in a schematic cartoon in Figure 8. It is clear that the EUV waves, especially WF1, play an essential role in linking the primary and sympathetic eruptions.

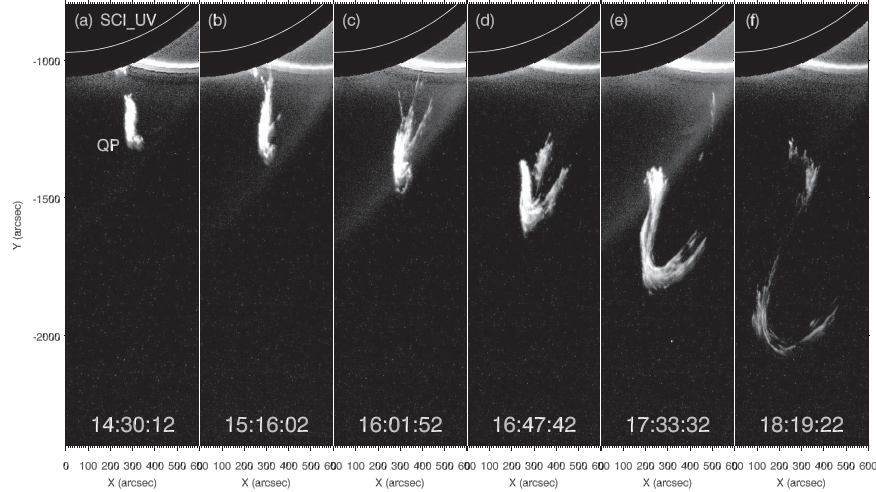


**Figure 6.** Rising QP observed by SCI\_UV during 14:30–18:20 UT. An online animation of the SCI\_UV images is available at [anim2.mp4](#). The  $\sim 13$  s animation covers from 14:30 UT to 18:30 UT.

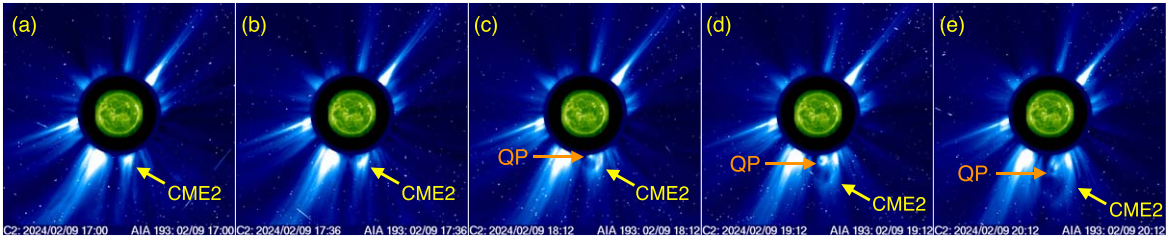


**Figure 7.** Original images observed by LASCO-C2 during 17:00–20:12 UT. The rising QP and bright front of CME2 are pointed out by orange and yellow arrows, respectively.

#### 4. Discussion

Kolotkov et al. (2016) proposed a model of the global transverse oscillations and stability of QPs, which are supported by magnetic dipoles. The periods of transverse oscillations with small amplitudes are derived analytically. Considering that LAOs are frequently observed (Hershaw et al. 2011; Shen et al. 2014a, 2014b; Dai et al. 2023), Kolotkov et al. (2018) investigated the effects of finite amplitudes on the transverse prominence oscillations. It is revealed that a metastable equilibrium of the prominence exists. The prominence is stable for small-amplitude displacements. However, it becomes unstable in the horizontal direction when the amplitude is large enough to exceed a threshold value. In our study of the transverse oscillation of QP, the maximal displacement amplitude reaches  $\sim 34$  Mm and the maximal velocity amplitude reaches  $\sim 143$  km s $^{-1}$ , which is close to the acoustic speed of the corona ( $T \sim 1.5$  MK) (see Figure 10 in Paper I). After the oscillation, QP starts to rise up and evolves into the bright core of CME2 (see Figure 7). Therefore, both the transverse oscillation and subsequent eruption of QP might

be explained by their analytical model. The large amplitudes of QP may exceed a threshold so that the prominence loses equilibrium and erupts, which provides a new piece of evidence for the conclusion that large-amplitude transverse oscillation is one of precursors for prominence eruptions (Chen et al. 2008).

A similar metastable equilibrium may exist for a longitudinally oscillating prominence as well. Using one-dimensional hydrodynamic numerical simulations with the MPI-AMRVAC code (Keppens et al. 2023), Zhang et al. (2013) carried out a parameter survey of longitudinal prominence oscillations along magnetic dipoles. It is found that the prominence is limited in the dipoles when the initial amplitudes are not so large. Nevertheless, a fraction of the prominence reaches and overshoots the shoulders of dipoles, leading to mass drainage along the legs of the prominence and a possible eruption when the initial amplitude is large enough (see their Figure 8). Fan (2020) performed 3D MHD simulations of large-amplitude, longitudinal oscillations of a prominence supported by a twisted coronal flux rope. It is revealed that the oscillations are quickly attenuated after a few cycles, which are followed by significant mass drainage and eventual eruption of the prominence. From this point of view, LAOs of prominences,

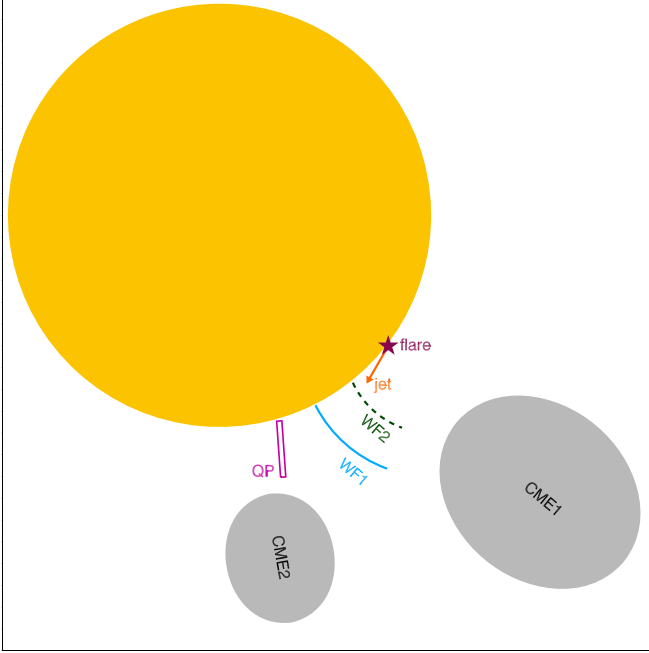


**Figure 8.** A schematic cartoon to illustrate the whole sequence of events on 2024 February 9.

including transverse and longitudinal polarizations, are considered as a conceivable precursor of prominence eruptions.

After developing a new technique for tracking CMEs in the FOV of LASCO, Sheeley et al. (1999) divided their sample into two types, gradual CMEs and impulsive CMEs. Impulsive CMEs are usually associated with flares and Moreton waves, while gradual CMEs are formed when prominences and their cavities rise up from below coronal streamers. Besides, impulsive CMEs are generally faster and tend to decelerate during propagation, while gradual CMEs are relatively slower and tend to accelerate. In Table 2, we compare the primary eruption and sympathetic eruption in detail. The former results from an HC eruption at 12:49 UT from AR 13575, while the latter results from a prominence eruption at  $\sim 14:10$  UT from the quiet region, which is delayed by  $\sim 80$  minutes. The HC eruption is characterized by a slow rise and a fast rise phase (Zhang et al. 2023, 2024), while the prominence eruption presents a constant acceleration ( $\sim 3.9 \text{ m s}^{-2}$ ). The primary eruption generates an X3.4 class flare, an impulsive CME, and EUV wave (WF1) as described in Section 2. WF1 serves as a causal link between the consecutive eruptions. It is noted that the prominence does not erupt instantly after the arrival of WF1. Instead, QP experiences a large-amplitude, transverse oscillation, which lasts for about one hour. The prominence becomes unstable after the oscillation and eventually erupts. The sympathetic eruption drives a gradual CME, whose leading edge shows a constant acceleration ( $\sim 6.5 \text{ m s}^{-2}$ ). The final speed of CME1 is almost 10 times higher than that of CME2. In brief, the primary and sympathetic

**Table 2**

Comparison Between the Primary Eruption and Sympathetic Eruption

Eruption	Primary	Sympathetic
Erupting structure	HC	QP
Source region	AR 13575	quiet region
Start time	12:49 UT	14:10 UT
Kinematics	slow rise and fast rise	constant acceleration
Flare	X3.4	...
CME	CME1	CME2
CME type	impulsive	gradual
CME speed [ $\text{km s}^{-1}$ ]	2782	277
EUV wave	WF1	...

eruptions exhibit remarkably different properties. Zhang et al. (2004) explored the kinematic properties of three CMEs associated with flares. It is found that there is close correlation both between the CME velocity and the SXR flux of the flare and between the CME acceleration and derivative of the SXR flux. In our study, CME2 undergoes continuous acceleration for nearly seven hours. However, it is not related to a flare underneath. In Figure 9, the left panel shows large-scale magnetic field lines obtained by the potential-field source surface (PFSS; Schatten et al. 1969; Schrijver & De Rosa 2003) modeling at 12:04 UT. The open and closed fields are indicated by magenta and white lines, respectively. The right panel shows the AIA 211 Å image at 13:09:45 UT. Close to the south polar region, the coronal hole (CH) is fainter than the surrounding quiet region and is associated with the footpoints of open field lines in the left panel. Since QP is also close to the south polar region, the slow CME is probably pushed by the fast solar wind during its propagation (Hassler et al. 1999; Tu et al. 2005).

Using He II 304 Å observations with the Full Sun Imager (FSI) of the Extreme Ultraviolet Imager (EUI; Rochus et al. 2020) onboard the Solar Orbiter (SoLO; Müller et al. 2020) mission, Mierla et al. (2022) reported a fast prominence eruption up to  $>6 R_{\odot}$  on 2022 February 15–16. The velocities of the leading edges of prominence and associated CME are  $\sim 1700$  and  $\sim 2200 \text{ km s}^{-1}$ , respectively. Using combined observations with the EUI/FSI in 174 Å and the SoLO/Metis (Antonucci et al. 2020) in visible light (VL) and UV ( $\text{Ly}\alpha$ ), Bemporad et al. (2022) studied a CME followed by a prominence eruption and a long current sheet on 2021 February 12. The prominence was tracked by Metis from  $\sim 3$  to  $\sim 5.4 R_{\odot}$ , while the early phase of the prominence was not observed due to the occulting disk. In our case, the prominence is completely tracked by ASO-S/SCI-UV from  $\sim 1.1$  to  $\sim 2.2 R_{\odot}$  in  $\text{Ly}\alpha$  wavelength, which is crucial to study the kinematics.

## 5. Summary

In this paper, we perform a follow-up investigation of the solar eruption originating from AR 13575 on 2024 February 9. The main results are summarized as follows:

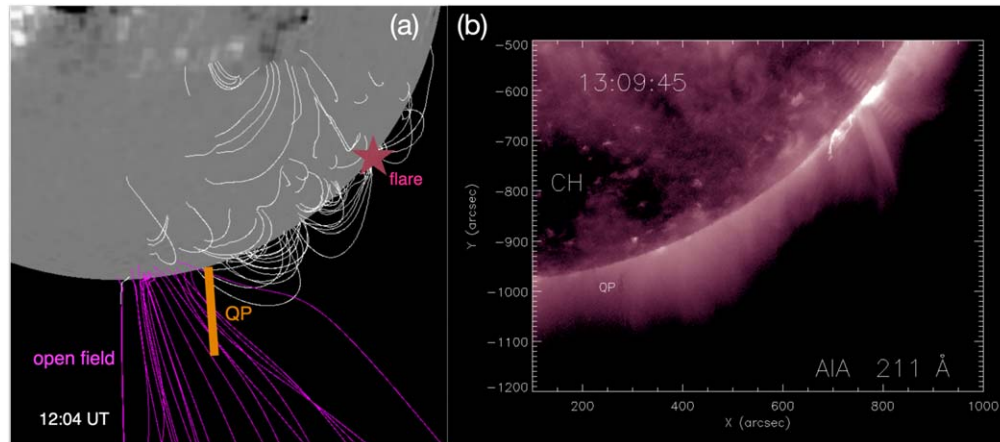


**Figure 9.** (a) Large-scale magnetic field lines obtained by the PFSS modeling at 12:04 UT on 2024 February 9. The open and closed fields are drawn with magenta and white lines, respectively. The flare and QP are signified by a red star and an orange stick respectively. (b) AIA 211 Å image at 13:09:45 UT, showing the dark CH and QP close to the south polar region.

1. The primary eruption of an HC results in an X3.4 class flare, a full-halo CME (CME1), and an EUV wave (WF1). Interaction between WF1 and QP leads to a large-amplitude, transverse oscillation of QP, which has been described in our previous paper (Paper I).
2. After the transverse oscillation, QP becomes unstable and lifts off. The rising motion of the prominence is clearly detected and tracked by GOES-16/SUVI until  $\sim 1.68 R_{\odot}$  and by LST/SCI\_UV onboard the ASO-S spacecraft until  $\sim 2.2 R_{\odot}$ . The velocity increases linearly from 12.3 to  $68.5 \text{ km s}^{-1}$  at 18:30 UT. The sympathetic eruption of QP drives the second CME (CME2) with a typical three-part structure. The bright core comes from the eruptive prominence, which could be tracked further until  $\sim 3.3 R_{\odot}$  by SOHO/LASCO-C2. The leading edge of CME2 accelerates continuously from  $\sim 120$  to  $\sim 277 \text{ km s}^{-1}$ .
3. The EUV wave serves as a causal link between the primary and sympathetic eruptions. The advantageous cadence and FOV of ASO-S/SCI\_UV provide a great opportunity to track an erupting prominence from  $\sim 1.1$  to  $\sim 2.2 R_{\odot}$  in  $\text{Ly}\alpha$  wavelength.

### Acknowledgments

The authors appreciate the reviewer for valuable suggestions that improved the quality of this article. We also thank Prof. Hui Li in Purple Mountain Observatory, Prof. Pengfei Chen in Nanjing University, and Prof. Xiaoli Yan in Yunnan Astronomical Observatories for helpful discussions. SDO is a mission of NASA's Living With a Star Program. AIA data are courtesy of the NASA/SDO science teams. This CME catalog is generated and maintained at the CDAW Data Center by NASA and The Catholic University of America in cooperation with the Naval

Research Laboratory. SOHO is a project of international cooperation between ESA and NASA. The ASO-S is supported by the Strategic Priority Research Program on Space Science, Chinese Academy of Sciences. This work is supported by the National Key R&D Program of China 2022YFF0503003 (2022YFF0503000), 2021YFA1600500 (2021YFA1600502), the Strategic Priority Research Program of the Chinese Academy of Sciences, grant No. XDB0560000, the National Natural Science Foundation of China (NSFC, grant Nos. 12373065, 12203102, 12403064, and 12403068), Natural Science Foundation of Jiangsu Province (BK20231510, BK20241707), the Project Supported by the Specialized Research Fund for State Key Laboratories, and Yunnan Key Laboratory of Solar Physics and Space Science under the grant No. YNSPCC202206.

### References

- Antonucci, E., Romoli, M., Andretta, V., et al. 2020, *A&A*, **642**, A10  
 Arregui, I., Oliver, R., & Ballester, J. L. 2018, *LRSP*, **15**, 3  
 Asai, A., Ishii, T. T., Isobe, H., et al. 2012, *ApJL*, **745**, L18  
 Bemporad, A., Andretta, V., Susino, R., et al. 2022, *A&A*, **665**, A7  
 Berger, T. E., Shine, R. A., Slater, G. L., et al. 2008, *ApJL*, **676**, L89  
 Bi, Y., Jiang, Y., Yang, J., et al. 2014, *ApJ*, **790**, 100  
 Brueckner, G. E., Howard, R. A., Koomen, M. J., et al. 1995, *SoPh*, **162**, 357  
 Carmichael, H. 1964, *NASSP*, **50**, 451  
 Chen, B., Feng, L., Zhang, G., et al. 2024, *SoPh*, **299**, 118  
 Chen, P. F. 2011, *LRSP*, **8**, 1  
 Chen, P. F., Innes, D. E., & Solanki, S. K. 2008, *A&A*, **484**, 487  
 Chen, P. F., Wu, S. T., Shibata, K., et al. 2002, *ApJL*, **572**, L99  
 Cheng, J.-X., Fang, C., Chen, P.-F., et al. 2005, *ChJAA*, **5**, 265  
 Cheng, X., Zhang, J., Ding, M. D., et al. 2013, *ApJL*, **769**, L25  
 Dacic, S., Török, T., Démoulin, P., et al. 2018, *ApJ*, **862**, 117  
 Dai, J., Zhang, Q., Qiu, Y., et al. 2023, *ApJ*, **959**, 71  
 Dai, J., Zhang, Q., Zhang, Y., et al. 2021, *ApJ*, **923**, 74  
 Darnel, J. M., Seaton, D. B., Bethge, C., et al. 2022, *SpWea*, **20**, e2022SW003044  
 Engvold, O. 1998, in IAU Coll. 167: New Perspectives on Solar Prominences, 150 (Aussais: ASP Conference Series), 23  
 Eto, S., Isobe, H., Narukage, N., et al. 2002, *PASJ*, **54**, 481

- Fan, Y. 2020, *ApJ*, 898, 34
- Feng, L., Li, H., Chen, B., et al. 2019, *RAA*, 19, 162
- Fletcher, L., Dennis, B. R., Hudson, H. S., et al. 2011, *SSRv*, 159, 19
- Forbes, T. G., Linker, J. A., Chen, J., et al. 2006, *SSRv*, 123, 251
- Gan, W., Zhu, C., Deng, Y., et al. 2023, *SoPh*, 298, 68
- Gan, W.-Q., Zhu, C., Deng, Y.-Y., et al. 2019, *RAA*, 19, 156
- Gilbert, H. R., Daou, A. G., Young, D., et al. 2008, *ApJ*, 685, 629
- Hassler, D. M., Dammasch, I. E., Lemaire, P., et al. 1999, *Sci*, 283, 810
- Hershaw, J., Foullon, C., Nakariakov, V. M., et al. 2011, *A&A*, 531, A53
- Hirayama, T. 1974, *SoPh*, 34, 323
- Hou, Y. J., Li, T., Song, Z. P., et al. 2020, *A&A*, 640, A101
- Illing, R. M. E., & Hundhausen, A. J. 1985, *JGR*, 90, 275
- Isobe, H., & Tripathi, D. 2006, *A&A*, 449, L17
- Jiang, Y., Yang, J., Hong, J., et al. 2011, *ApJ*, 738, 179
- Jing, J., Lee, J., Spiro, T. J., et al. 2003, *ApJL*, 584, L103
- Joshi, N. C., Schmieder, B., Magara, T., et al. 2016, *ApJ*, 820, 126
- Kaiser, M. L., Kucera, T. A., Davila, J. M., et al. 2008, *SSRv*, 136, 5
- Keppens, R., Popescu Braileanu, B., Zhou, Y., et al. 2023, *A&A*, 673, A66
- Kolotkov, D. Y., Nisticò, G., & Nakariakov, V. M. 2016, *A&A*, 590, A120
- Kolotkov, D. Y., Nisticò, G., Rowlands, G., et al. 2018, *JASTP*, 172, 40
- Kopp, R. A., & Pneuman, G. W. 1976, *SoPh*, 50, 85
- Lemen, J. R., Title, A. M., Akin, D. J., et al. 2012, *SoPh*, 275, 17
- Li, D., Shen, Y., Ning, Z., et al. 2018, *ApJ*, 863, 192
- Li, H., Chen, B., Feng, L., et al. 2019, *RAA*, 19, 158
- Lin, Y. 2011, *SSRv*, 158, 237
- Liu, R., Liu, C., Xu, Y., et al. 2013, *ApJ*, 773, 166
- Luna, M., Joshi, R., Schmieder, B., et al. 2024, *A&A*, 691, A354
- Luna, M., Karpen, J., Ballester, J. L., et al. 2018, *ApJS*, 236, 35
- Lynch, B. J., & Edmondson, J. K. 2013, *ApJ*, 764, 87
- Mackay, D. H., Karpen, J. T., Ballester, J. L., et al. 2010, *SSRv*, 151, 333
- Martin, S. F. 1998, *SoPh*, 182, 107
- Mierla, M., Zhukov, A. N., Berghmans, D., et al. 2022, *A&A*, 662, L5
- Moreton, G. E. 1960, *AJ*, 65, 494
- Müller, D., St. Cyr, O. C., Zouganelis, I., et al. 2020, *A&A*, 642, A1
- Ni, Y. W., Guo, J. H., Zhang, Q. M., et al. 2022, *A&A*, 663, A31
- Ning, Z., Cao, W., Okamoto, T. J., et al. 2009, *A&A*, 499, 595
- Okamoto, T. J., Tsuneta, S., Berger, T. E., et al. 2007, *Sci*, 318, 1577
- Oliver, R., & Ballester, J. L. 2002, *SoPh*, 206, 45
- Parenti, S. 2014, *LRSP*, 11, 1
- Patsourakos, S., & Vourlidias, A. 2009, *ApJL*, 700, L182
- Pesnell, W. D., Thompson, B. J., & Chamberlin, P. C. 2012, *SoPh*, 275, 3
- Qiu, Y., Li, C., Guo, Y., et al. 2024, *ApJL*, 961, L30
- Rochus, P., Auchère, F., Berghmans, D., et al. 2020, *A&A*, 642, A8
- Schatten, K. H., Wilcox, J. M., & Ness, N. F. 1969, *SoPh*, 6, 442
- Schrijver, C. J., & De Rosa, M. L. 2003, *SoPh*, 212, 165
- Seaton, D. B., & Darnel, J. M. 2018, *ApJL*, 852, L9
- Sheeley, N. R., Walters, J. H., Wang, Y.-M., et al. 1999, *JGR*, 104, 24739
- Shen, Y., Ichimoto, K., Ishii, T. T., et al. 2014a, *ApJ*, 786, 151
- Shen, Y., Liu, Y., & Su, J. 2012, *ApJ*, 750, 12
- Shen, Y., Liu, Y. D., Chen, P. F., et al. 2014b, *ApJ*, 795, 130
- Song, H., Li, L., & Chen, Y. 2022, *ApJ*, 933, 68
- Song, Z., Hou, Y., Zhang, J., et al. 2020, *ApJ*, 892, 79
- Sterling, A. C., & Moore, R. L. 2004, *ApJ*, 613, 1221
- Sturrock, P. A. 1966, *Natur*, 211, 695
- Tadikonda, S. K., Freesland, D. C., Minor, R. R., et al. 2019, *SoPh*, 294, 28
- Thompson, B. J., Plunkett, S. P., Gurman, J. B., et al. 1998, *GeoRL*, 25, 2465
- Titov, V. S., Mikic, Z., Török, T., et al. 2012, *ApJ*, 759, 70
- Török, T., Panasenco, O., Titov, V. S., et al. 2011, *ApJL*, 739, L63
- Tripathi, D., Isobe, H., & Jain, R. 2009, *SSRv*, 149, 283
- Tu, C.-Y., Zhou, C., Marsch, E., et al. 2005, *Sci*, 308, 519
- Vršnak, B., Veronig, A. M., Thalmann, J. K., et al. 2007, *A&A*, 471, 295
- Wang, D., Liu, R., Wang, Y., et al. 2018, *ApJ*, 869, 177
- Wang, J., Li, D., Li, C., et al. 2024, *ApJL*, 965, L28
- Wang, R., Liu, Y. D., Zimovets, I., et al. 2016, *ApJL*, 827, L12
- Xue, J.-c., Feng, L., Li, H., et al. 2024, *SoPh*, 299, 89
- Yang, J., Jiang, Y., Zheng, R., et al. 2012, *ApJ*, 745, 9
- Zhang, J., Dere, K. P., Howard, R. A., et al. 2004, *ApJ*, 604, 420
- Zhang, Q., Ou, Y., Huang, Z., et al. 2024, *ApJ*, 977, 4
- Zhang, Q., Teng, W., Li, D., et al. 2023, *ApJ*, 958, 85
- Zhang, Q. M., Chen, J. L., Li, S. T., et al. 2022, *SoPh*, 297, 18
- Zhang, Q. M., Chen, P. F., Xia, C., et al. 2012, *A&A*, 542, A52
- Zhang, Q. M., Chen, P. F., Xia, C., et al. 2013, *A&A*, 554, A124
- Zhang, Q. M., Guo, J. H., Tam, K. V., et al. 2020, *A&A*, 635, A132
- Zhang, Q. M., Li, T., Zheng, R. S., et al. 2017, *ApJ*, 842, 27
- Zhang, Q. M., Lin, M. S., Yan, X. L., et al. 2024, *MNRAS*, 533, 3255
- Zhang, Y., Zhang, Q., Song, D.-. chao, et al. 2024, *ApJ*, 963, 140
- Zheng, R., Zhang, Q., Chen, Y., et al. 2017, *ApJ*, 836, 160
- Zhou, C., Shen, Y., Zhou, X., et al. 2021, *ApJ*, 923, 45
- Zhou, Y., Ji, H., & Zhang, Q. 2023, *SoPh*, 298, 35